mater.scichina.com link.springer.com

Published online 20 February 2024 | https://doi.org/10.1007/s40843-023-2749-3
Sci China Mater 2024, 67(3): 852–862

A universal strategy for narrowband organic photodetectors enabling arbitrary narrow spectrum detection

Yu Zhu[1], Hao Qin[1], Tingting Guo[1], Yanqing Yang[1], Zhe Zhang[1], Jing Zhang[1], Mingpeng Li[1], Hongbin Chen[1], Simin Wu[1], Ruiman Han[1], Xiangjian Wan[1], Guanghui Li[1*] and Yongsheng Chen[1,2*]

ABSTRACT **Narrowband photodetectors (PDs) with remarkable comprehensive performance are extensively in demand in critical applications such as spectrometers, light detection and ranging (LiDAR), optical communication, and surveillance. Despite the fact that silicon-based narrowband PDs currently predominate the market, their inherent rigidity, fixed band limitations, and bulky sizes significantly impede their applications in emerging fields, particularly in flexible and wearable optoelectronics. In this work, a facile and universal solution-processed strategy is presented to fabricate narrowband organic PDs (OPDs) that can detect arbitrary narrow spectra, which is realized by introducing an independent organic optical adjusting layer (OAL) comprising the same donor and acceptor within the photoactive film of OPD. With this strategy, we successfully fabricate a narrowband OPD centered at 750 nm, with a full width at half-maximum (FWHM) of 40 nm, spectral responsivity ratio of 3667, and −3 dB cutoff frequency of 927 kHz, as recorded in self-powered narrowband OPDs. Notably, this novel OAL strategy shows outstanding universality across all OPDs for detecting arbitrary narrow spectra in the range of 600–1000 nm with tunable FWHMs (minimum narrowing step of 2 nm), high responsivity and detectivity, and fast response speed. Benefiting from the inherent flexibility of organic semiconductors, we fabricate a flexible and bendable narrowband near-infrared OPD linear array for omnidirectional LiDAR, realizing a 360° horizontal scan without mechanical rotation.**

Keywords: organic photodetector, narrowband organic photodetector, LiDAR, flexible photodetector, visible-near-infrared narrowband organic photodetector

INTRODUCTION

Narrowband photodetectors (PDs), which enable highly accurate and selective specific spectral detection, are the basic pillar of sophisticated optical systems widely utilized in various fields [1–4], such as light detection and ranging (LiDAR) [5–7], spectrometers [8–10], imaging [11–13], solar-blind communication [14–16], surveillance [17], and military defense [16]. An ideal narrowband PD with significant commercial prospects should simultaneously have remarkable comprehensive optoelectronic performance and meager cost [18,19], including (i) tunable and narrow full width at half-maximum (FWHM) at the desired response window, (ii) high spectral rejection ratio (SRR) and detectivity, fast response, and low power consumption [20], and (iii) high compatibility with future mobile and flexible devices, miniature size with simple device architecture, and economical manufacturing process [21,22]. Traditionally, the state-of-the-art commercial narrowband PDs commonly have an architecture that predominantly combines fixed-band inorganic PDs with bulky optical modules, such as dichroic prisms, optical filters, and narrowband absorbers, to achieve target spectrum discrimination [23–25]. Despite achieving significant progress with these pioneering studies, they commonly suffer from drawbacks such as complicated architecture [26,27], bulky and rigid size, and low photon efficiency, which hinder their applications in emerging fields, particularly in the ever-growing flexible and wearable electronic industry that requires highly selective and sensitive wavelength discrimination *via* a highly flexible, lightweight, and compact detection system [1,21,28,29].

Organic semiconductors utilized in organic PDs (OPDs) show outstanding superiorities, such as high absorption coefficients ($>10^5$ cm^{-1}) [23], tunable bandgaps, and intrinsic flexibility [30–32], enabling efficient light absorption within a few hundred nanometers of thickness. Despite noteworthy strategies, such as the photomultiplication effect, charge collection narrowing effect, and charge injection narrowing [33,34], which have been successfully developed for detecting narrow wavelengths with high specific parameters, the sensitivity and response speed of these narrowband OPDs still lag far behind those of thin-film OPDs operating in self-powered mode. The fundamental reason for this is the high exciton binding energy and short exciton diffusion length of organic semiconductors, which limits the thickness of OPDs to 100–200 nm and shows significant challenges in obtaining high-performance narrowband OPDs. Recently, self-filtering narrowband OPDs (SF-OPDs) are a straightforward and effective tool to suppress background light interference, which enables specific light detection with FWHMs less than 40 nm [3,35,36]. However, SF-OPDs generally suffer

[1] The Centre of Nanoscale Science and Technology and Key Laboratory of Functional Polymer Materials, Institute of Polymer Chemistry, Tianjin Key Laboratory of Functional Polymer Materials, College of Chemistry, and Renewable Energy Conversion and Storage Center (RECAST), Nankai University, Tianjin 300071, China
[2] State Key Laboratory of Elemento-Organic Chemistry, Nankai University, Tianjin 300071, China
[*] Corresponding authors (emails: yschen99@nankai.edu.cn (Chen Y); ghli1127@nankai.edu.cn (Li G))

from slow response speeds because of the thick photoactive film and the complicated multiple-step fabrication process. When the thick photoactive film is removed from the inside of OPD, it becomes an independent and electrically isolated layer without involvement in any charge dynamic activity in OPDs, thus maintaining the critical figures-of-merit of thin-film OPDs. Although a wide variety of commercial organic dyes exhibit immense potential in optical filters for narrowband OPDs, it is still demanding to precisely tune the FWHM, response window, and responsivity when integrating with OPDs. Resolving these problems to achieve arbitrary narrow FWHMs and concurrently maintain high sensitivity and response speed for ideal OPDs across the visible (400 nm) to near-infrared II (NIR-II) (1000 nm) spectrum remains a substantial challenge, particularly for narrowband OPDs with FWHMs ≤ 40 nm, responsivity over 0.2 A W^{-1}, SRR above 1000, and −3 dB cutoff frequency above 300 kHz.

In this contribution, a universal and facile solution-processed strategy was developed for arbitrary narrowband spectrum detection from the visible to NIR-II regions. The narrowband OPDs were constructed by introducing a blend of donor (D) and acceptor (A) that act as both a photoactive material and an independent organic optical adjusting layer (OAL) stacked on the OPD to precisely manipulate the FWHM, sensitivity, and response window. With this strategy, a narrowband OPD centered at 750 nm was successfully achieved with outstanding comprehensive performance, including a narrow FWHM of less than 40 nm, high responsivity of 0.28 A W^{-1}, SRR of 3667, specific detectivity of 10^{12} Jones, and −3 dB cutoff bandwidth of 927 kHz at 750 nm, ranking the highest values among self-powered narrowband OPDs in the literature. By tuning the D:A weight ratio of the OAL film, we successfully achieved tunable FWHMs from 80 to 30 nm with a minimum narrowing step of 2 nm to satisfy practical requirements. In addition, this novel OAL strategy shows remarkable universality to all self-powered OPDs for arbitrary narrow spectral detection in the range of 600–1000 nm with outstanding performance, overcoming trade-offs in SRR, FWHM, response speed, responsivity, and driving bias in narrowband OPDs. By systematically exploring the underlying mechanism of OAL-OPDs, we proposed material selection guidelines and device strategies for designing narrowband OPDs for arbitrary wavelength discrimination. Moreover, a flexible narrowband NIR OPD linear array centered at 950 nm was fabricated for omnidirectional LiDAR, which can horizontally scan 360° without mechanical rotation, detecting up to 60 m without visible light interference. We envisage that the developed facile and effective strategy, along with the solution fabrication techniques, will motivate a new generation of high-performance flexible narrowband OPDs for emerging applications and speed up their commercialization.

EXPERIMENTAL SECTION

Materials

Polymeric donor poly[(2,6-(4,8-bis(5-(2-ethylhexyl-3-fluoro)-thiophen-2-yl)-benzo[1,2-*b*:4,5-*b*′]dithiophene))-alt-5,5′-(5,8-bis(4-(2-butyloctyl)thiophen-2-yl)dithieno[3′,2′:3,4;2″,3″:5,6]-benzo[1,2-*c*][1,2,5]thiadiazole)] (D18), poly[(2,6-(4,8-bis(5-(2-ethylhexyl)thiophen-2-yl)-benzo[1,2-*b*:4,5-*b*′]dithiophene))-alt-(5,5-(1′,3′-di-2-thienyl-5′,7′-bis(2-ethylhexyl)benzo[1′,2′-*c*:4′,5′-*c*′]dithiophene-4,8-dione)] (PBDB-T), and poly[(2,6-(4,8-bis(5-(2-ethylhexyl-3-fluoro)thiophen-2-yl)-benzo[1,2-*b*:4,5-*b*′]dithiophene))-alt-(5,5-(1′,3′-di-2-thienyl-5′,7′-bis(2-ethylhexyl)benzo-[1′,2′-*c*:4′,5′-*c*′]dithiophene-4,8-dione)] (PM6) were procured from Solarmer Material (Beijing) Inc., and PCE-10 was obtained from 1-Materials Inc. $PC_{71}BM$ was bought from Libra Technology Co., Ltd. F(Br)-ThCl, F-M, F-2F, FO-2Cl, and CH17 were synthesized using our published method [37–40]. F8IC and SiOTIC were procured from Zhiyan Technology Co., Ltd. Chlorobenzene, chloroform chloronaphthalene, 1,8-diiodooctane (DIO), and $Zn(CH_3COO)_2$ were purchased from Sigma-Aldrich. *N*,*N*′-Bis(*N*,*N*-dimethylpropan-1-amine oxide)-perylene-3,4,9,10-tetracarboxylic diimide (PDINO) and poly-(9,9-bis(3′-(*N*,*N*-dimethyl)-*N*-ethylammoinium-propyl-2,7-fluorene)-alt-2,7-(9,9-dioctylfluorene))dibromide (PFN-Br) were obtained from eFlexPV Limited and Seniormaterial, respectively. All other reagents and chemicals used in this work were purchased from commercial suppliers and were directly used without further purification. Indium tin oxide (ITO)/glass transparent electrodes and ITO/polyethylene terephthalate (PET) substrates were obtained from Advanced Election Technology Co., Ltd. and Xiangchen Technology, respectively.

Device fabrication

OPDs based on PBDB-T:F-2F (λ_{peak} = 750 nm) were fabricated with an architecture of glass/ITO/ZnO/PFN-Br/PBDB-T:F-2F/MoO*x*/Ag. First, the glass/ITO substrate was sequentially pre-cleaned in an ultrasonic bath of detergent, deionized water, acetone, and isopropanol, respectively. Afterward, the ITO substrate was irradiated under ultraviolet (UV) light in an UV-ozone chamber (Jelight Company) for 15 min, followed by spin coating a layer of ZnO precursor. The ITO with ZnO precursor was annealed at 200°C for 1 h in air to obtain the ZnO film. Subsequently, a thin layer of PFN-Br was spin-coated on the ZnO layer. Then, the blend solution of D18:$PC_{71}BM$ (1:1 *w*/*w*, 9 mg mL^{-1}, chlorobenzene) was spin-coated at 2000 r min^{-1} for 40 s to prepare the active layer. A MoO*x* layer (6 nm) and an Ag layer (110 nm) were then deposited on the active layer by vacuum evaporation at 2 × 10^{-4} Pa. Finally, the OAL layer containing PBDB-T:F-2F (10:0.5, 10:1, 10:2, 10:3, 10:4, 10:5, 10:6, 20 mg mL^{-1} in chlorobenzene, refer to PBDB-T:F-2F) was spin-coated for 30 s on the backside of the ITO glass in the OPD. See the Supplementary information for device fabrication of narrowband detectors in other bands.

Device characterizations

Dark current–voltage (*J*–*V*) and photocurrent–time (*I*–*T*) curves of the devices were collected using a semiconductor parameter analyzer (Keysight B1500A). The external quantum efficiency (EQE) and responsivity spectra were recorded using a QE-R Solar Cell Spectral Response Measurement System (Enli Technology Co., Ltd., Taiwan). Response time and −3 dB cutoff frequency were determined using a high-resolution oscilloscope (MDO4104C, Tektronix) through modulating light-emitting diodes (LEDs) controlled by a signal generator (DG990, RIGOL) in square-wave mode. LED spectra were collected using a spectrometer (USB4000, Ocean Optics). The refractive index and extinction coefficient of materials were determined using an ellipsometer (Horoba UVISEL PLUS).

The optical field distribution and profile of the photogenerated charge carriers in OPDs were simulated using the finite-difference time domain (COMSOL).

LiDAR measurement

Omnidirectional LiDAR was performed by illuminating the target object *via* a laser diode (900 nm, 10 W) and then collecting the reflected light signal from the object *via* OAL-OPD. The laser diode was controlled by a signal generator (DG990, RIGOL) operated in square-wave mode. The reflected light signal was amplified by a preamplifier into the oscilloscope. The setup of the LiDAR system is illustrated in Supplementary information. The distance was calculated using $R = c\frac{\Delta\tau}{2}$, where R is the distance between the laser and object, c is the light speed, and τ is the round-trip time of flight (TOC) between the transmission of an outgoing laser pulse and the arrival at the receiver of the pulse [6].

RESULTS AND DISCUSSION

Optoelectronic performance of narrowband OPDs based on PBDB-T:F-2F

Fig. 1a shows the schematic cross-sectional view and working principle of the OAL-type narrowband OPD that consists of an OPD with a bulk heterojunction (BHJ) structure and a layer of OAL stacked on top of the OPD. Here, the thick OAL (300–500 nm) comprises the same D:A blend used in the OPD but different weight ratios. In the OAL-OPD, high-energy photons entering the thick OAL are entirely absorbed by the wide-bandgap donors, whereas low-energy photons can penetrate the OAL and excite the rear OPD because of the relatively low absorption coefficient at the absorption tail of the OAL. When the acceptor weight ratio is increased, the OAL absorbs more long-wavelength photons, leading to a red shift of the response window and narrowing the FWHM. To simultaneously realize a narrow FWHM and high responsivity, it demands synergy between the OAL with a suitable absorption profile and the OPD with a high EQE. Unlike the reported thick-junction narrowband OPDs that need fine-tuning of the BHJ film composition and thickness [3], the OAL-OPD can be readily fabricated by directly spin-coating or blade-coating the OAL solution on the transparent electrode side of the OPD without additional treatment, facilitating the large-scale preparation of narrowband OPDs.

To precisely tune the FWHMs, OAL-OPDs were fabricated using PBDB-T:F-2F-based OALs with different weight ratios of 10:0.5 (OAL-OPD-1), 10:1 (OAL-OPD-2), 10:2 (OAL-OPD-3), 10:3 (OAL-OPD-4), and 10:4 (OAL-OPD-5). Fig. 1b presents the chemical structures of PBDB-T and F-2F used in the OAL-OPDs, which show complementary optical absorption in the range of 400–770 nm (Fig. 1c). The detailed process of OPD, OAL, and OAL-OPD fabrication and optimization are described in the EXPERIMENTAL SECTION. Besides a high EQE of 80% from 550 to 750 nm, the F-2F-based OPD shows a sharp EQE edge, which can contribute to a narrow FWHM and improved

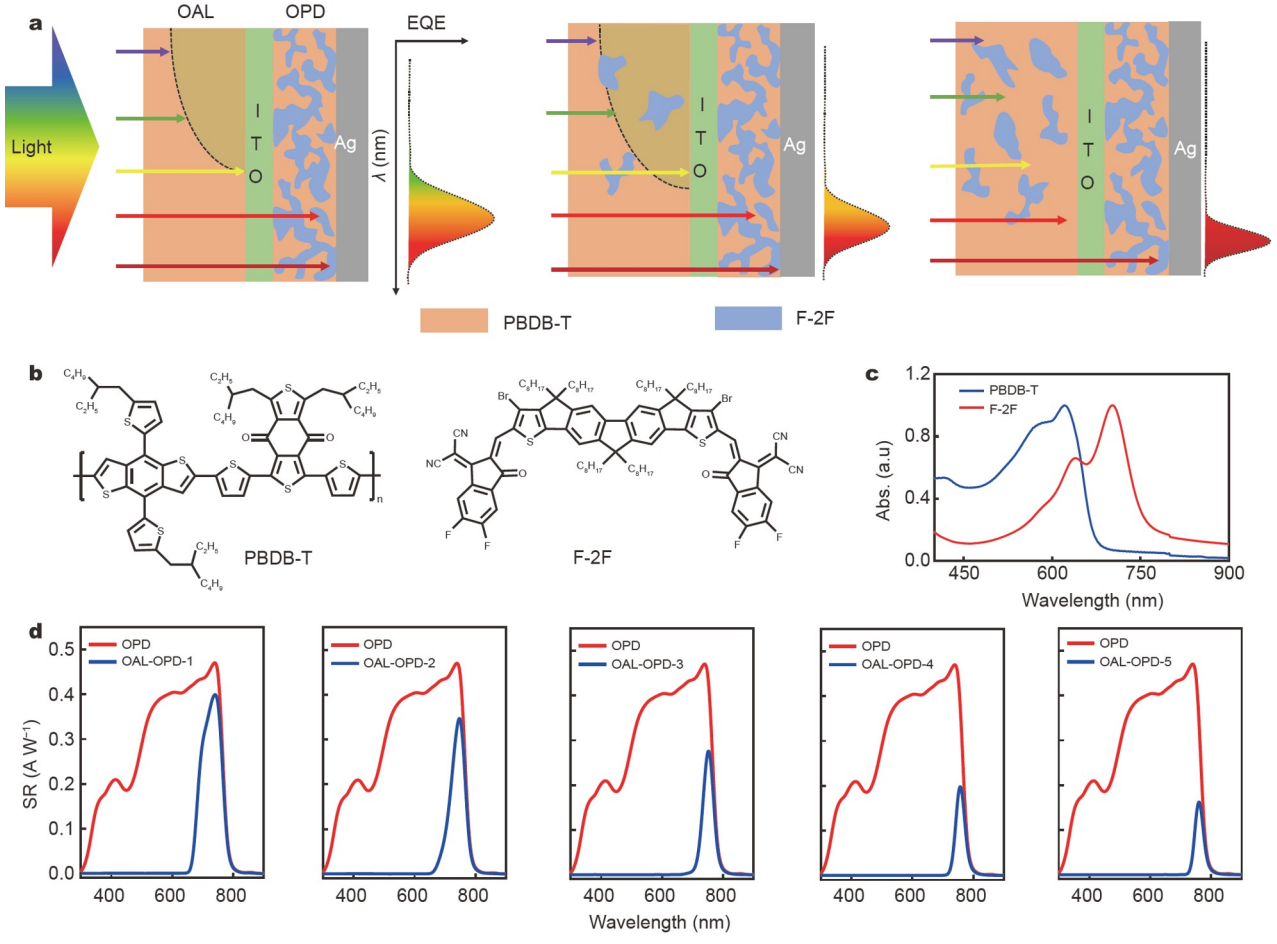

Figure 1 Device structure and material characterizations. (a) Schematic and working principle of OAL-type narrowband OPDs. (b) Chemical structures of PBDB-T and F-2F. (c) Optical absorption profiles of PBDB-T and F-2F. (d) Responsivities of OPDs and OAL-OPDs with different OALs.

OAL-OPD responsivity (Fig. 1d). In Fig. S1 and Table S1, the absorption tail of OALs demonstrates a red-shifting absorption onset and a shaper slope of the absorption edge with increasing F-2F weight ratio. Thus, the corresponding OAL-OPDs show gradually narrowing FWHMs with a dominant peak response centered at 750 nm (Fig. 1d). In addition, as more low-energy photons are absorbed by OALs with higher fractions of F-2F molecules, the peak response positions of OAL-OPDs demonstrate a slight red shift from 740 to 770 nm, which is consistent with the above assumption. The detailed results of the OAL-OPDs, i.e., responsivities, FWHMs, and response positions, are discussed below.

Dark current is a critical measure of OPDs that determines the noise level, specific detectivity (D^*), and linear dynamic range (LDR). As most narrowband OPDs in the literature have been constructed with thick BHJ films with unbalanced D:A weight ratios and large amounts of trap states, they commonly operate under high driving bias (>10 V) for efficient charge transport, thus leading to high charge injection, dark current, and large shot noise [34,41]. The optimized OAL-OPDs based on the F-2F acceptor demonstrate an extremely low dark current of 6.8 pA cm^{-2} at zero bias, as shown in Fig. 2a. Here, the OAL is electrically isolated from the OPD, which is not involved in charge generation and transport in the photoactive film. Thus, the OAL-OPD maintains the advantages of thin-film OPDs, such as small dark currents, low shot noise, and self-powered characteristics. Moreover, the OPD was fabricated with a thin BHJ film comprising a donor and an acceptor with suitable energetic levels, rational weight ratios, and balanced electron/hole mobilities, which can efficiently reduce the thermally excited charge generation and recombination in the dark, resulting in a low dark current [3].

As depicted in Fig. 2b, the OAL-OPD displays a distinctly gradually narrowed FWHM from 80 to 30 nm with increasing PBDB-T:F-2F weight ratios of OALs from 10:0.5 to 10:6. Correspondingly, the responsivity decreases from 0.4 to 0.13 A W^{-1}. Hence, it is highly possible to fine-tune the FWHMs of OAL-OPDs by precisely manipulating the weight ratios of the acceptors in OALs, satisfying the practical requirements. The narrowing step of the FWHM can reach as low as 2 nm. To assess the comprehensive performance of OAL-OPDs with respect to responsivities and FWHMs, we introduced the

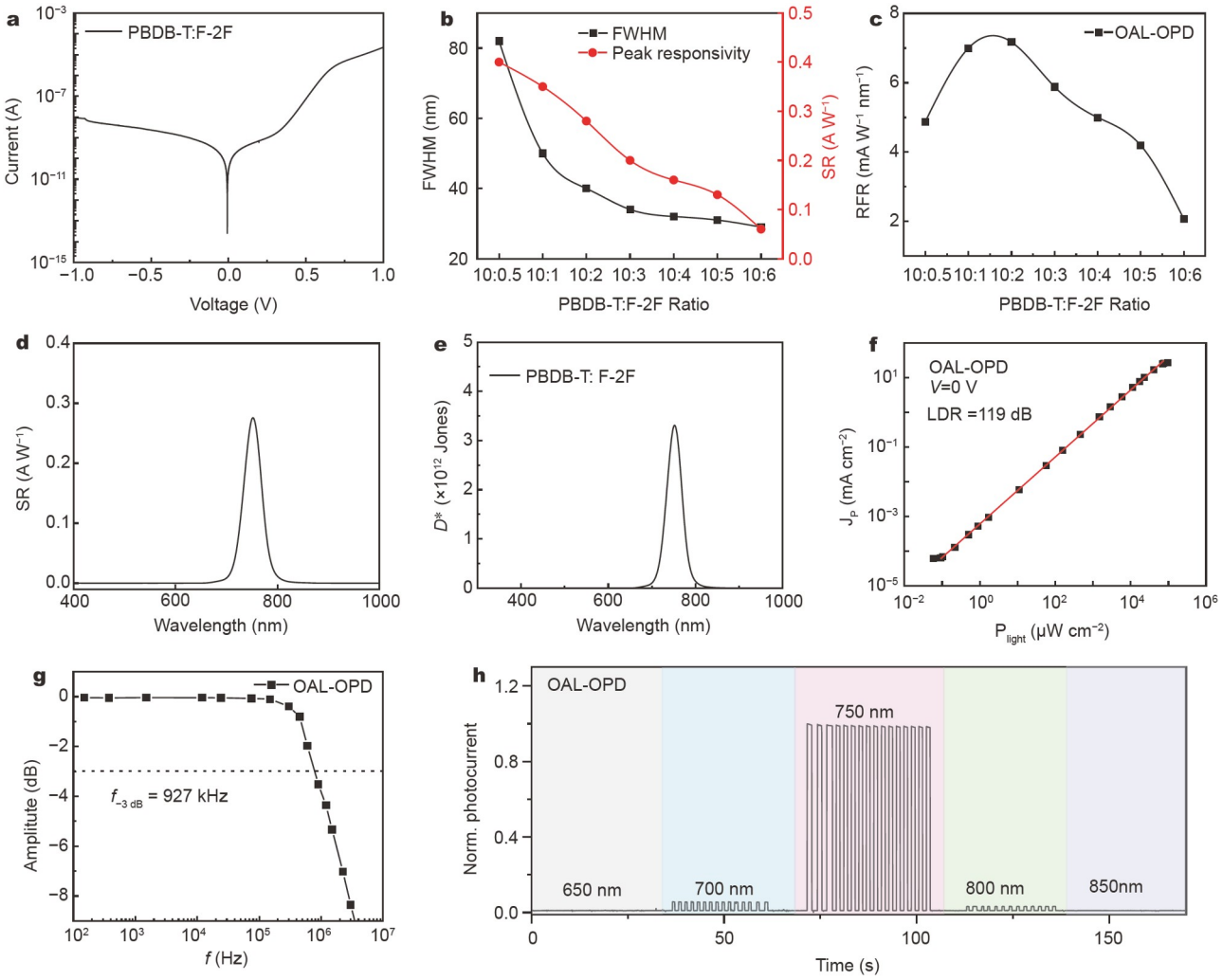

Figure 2 Optoelectronic performance of OAL-OPDs prepared with PBDB-T:F-2F. (a) J–V curve of OAL-OPD in the dark. (b) Summary of FWHMs and responsivities of OAL-OPDs with different OALs. (c) RFRs of OAL-OPDs. Responsivity (d), specific detectivity (e), LDR (f), and −3 dB cutoff frequency (g) of OAL-OPD with an FWHM of 40 nm. (h) Photoresponse of OAL-OPD under light irradiation at different wavelengths of 650, 700, 750, 800, and 850 nm.

responsivity FWHM ratio (RFR) as a crucial parameter, which is defined as the ratio of peak responsivity (R) to the FWHM and expressed as follows:

$$\mathrm{RFR}=\frac{R_{\mathrm{Peak}}}{\mathrm{FWHM}}. \quad (1)$$

As displayed in Fig. 2c, the OAL-OPD with an FWHM of 40 nm has the highest RFR of 7 mA W^{-1} nm^{-1} with a responsivity of 0.28 A W^{-1}. Thus, the optimized OAL-OPD with an FWHM of 40 nm was chosen to examine all the critical figures-of-merit of OAL-OPDs.

The SRR is a critical figure-of-merit for describing the ability of PDs to distinguish narrowband photons from those of broad spectra and is given by [42]

$$\mathrm{SRR}=\frac{\text{Narrowband spectral response}}{\text{Wideband spectral response}}. \quad (2)$$

The OAL-OPD with an FWHM of 40 nm shows a high SRR of 3667, ranking as the highest among self-powered OPDs. Because organic semiconductors with high absorption coefficients in the OAL can fully absorb the short wavelength, the OAL-OPD demonstrates an ultraweak response in this region, resulting in a high SRR for OAL-OPDs. In Fig. 2d, the OAL-OPD with an FWHM of 40 nm displays a symmetrical response shape centered at 750 nm.

Specific detectivity (D^*) is generally employed to assess the sensitivity and capability of ultraweak light detection in OPDs and is calculated using

$$D^* = \frac{R\sqrt{AB}}{i_n}, \quad (3)$$

where R, A, B, and i_n are the responsivity, effective area, bandwidth, and noise current, respectively. The self-powered OAL-OPD with an FWHM of 40 nm has a high D^* value of 3.3×10^{12} Jones centered at 750 nm, as shown in Fig. 2e. The LDR of the OAL-OPD spans over 119 dB, covering a light intensity range from 10^{-7} to 10^{-1} W cm^{-2} at 750 nm, depicting that the responsivity of the OAL-OPD remains consistent under a broad range of incident light power (Fig. 2f). Such outstanding performance is ascribed to the low dark current and high responsivity of the OAL-OPD.

Response speed is one of the most significant merits and plays a critical role in OPDs for applications such as LiDAR systems, high-speed imaging/video, and optical communication. The photodetection speed of the OAL-OPD was characterized based on the rise/fall time (10%–90%) averaged around 600 ns, which is one order of magnitude higher than previous narrowband OPDs with different working mechanisms. Moreover, the corresponding −3 dB cutoff frequency is 927 kHz at zero bias, as displayed in Fig. 2g. This exceptional response speed can be ascribed to the high and balanced charge mobility and short charge transit length in the OAL-OPD, which enables efficient exciton separation and fast charge transport to electrodes, resulting in high-speed photoresponse. To further explore the spectral selectivity of the OAL-OPD based on PBDB-T:F-2F, an I–T curve was constructed by using pulse light irradiation under different wavelengths with the same light intensities. In Fig. 2h, the OAL-OPD with an FWHM of 40 nm displays a significant response under illumination of 750 nm (10 μW cm^{-2}), whereas rather faint responses are observed in the spectra of 650, 700, 800, and 850 nm. In conclusion, the OAL-OPD with a simple architecture keeps the advantages of the original OPDs, i.e., low dark current, fast response, low driving bias, and high responsivity.

Working mechanism of OAL-OPDs

To study the optical distribution in OAL and BHJ films, we

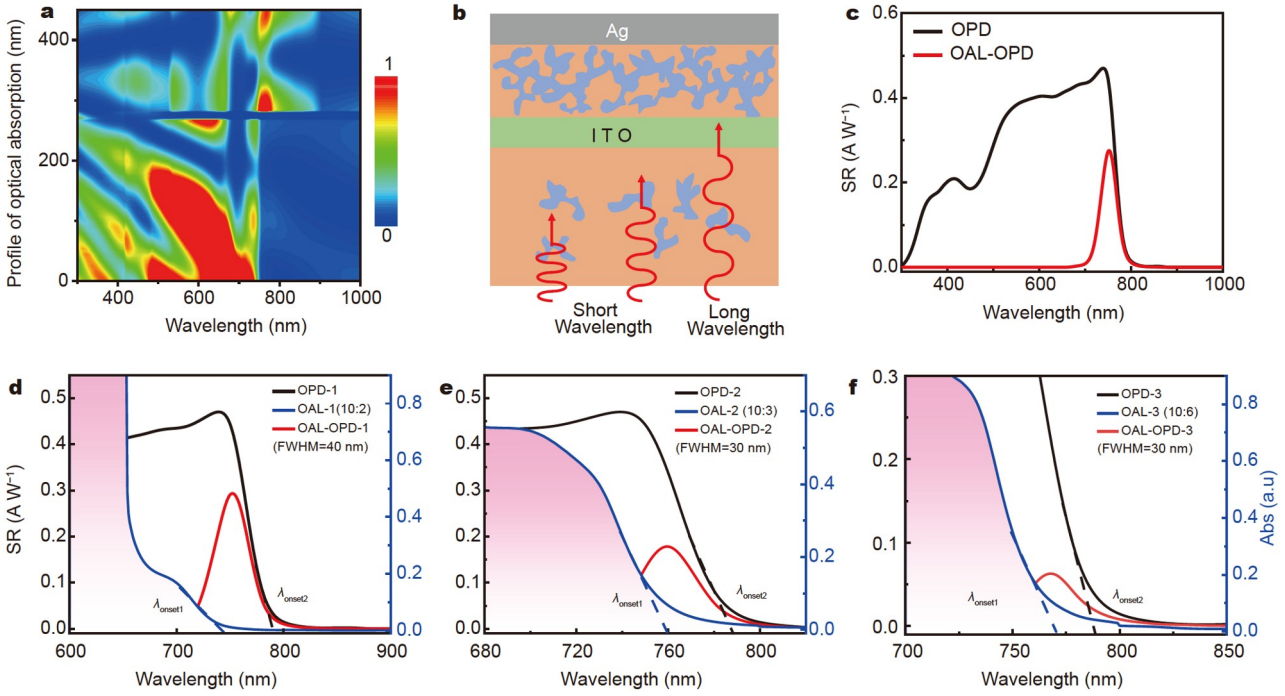

Figure 3 Absorption simulation and performance of tunable narrowband OPDs based on PBDB-T:F-2F. (a) Simulated spectrally and spatially resolved light absorption profile of PBDB-T:F-2F-based OPD and OAL with a weight ratio of 10:2 and thickness of 300 nm. (b) Schematic of light absorption with different wavelengths in the OAL and OPD. (c) Responsivities of OPD and OAL-OPD (FWHM = 40 nm) based on PBDB-T:F-2F. Photoresponses of OPDs and OAL-OPDs with different OALs: (d) FWHM = 40 nm, (e) FWHM = 30 nm, and (f) FWHM = 30 nm.

performed simulations to visualize the spectrally and spatially resolved photon absorption profile of the PBDB-T:F-2F (10:2) blend in 300 nm-thick OAL, as shown in Fig. 3a. Obviously, the light (λ < 700 nm) penetration depth in OAL with PBDB-T:F-2F is relatively shallow because of the high absorption eco-efficiency of the film, and most of the incident photons under 700 nm are fully absorbed illustrated in Fig. 3b. However, the incident light with long wavelengths of 700–800 nm can penetrate the OAL and reach the rear BHJ film, resulting in the excitation of the F-2F acceptor and generation of free charges in the OPD, consistent with the responsivity of the OAL-OPD (Fig. 3c).

Unlike previous narrowband OPDs that manipulate exciton separation, free charge transport, and charge collection within thick BHJ films for specific spectrum detection [3,34], in this work, the OAL-OPD attains ultra-narrowband photodetection by controlling the incident photons arriving at the OPD by tuning the optical characteristics of the OAL. In an OPD with a fixed response spectrum, the absorption profiles of OALs play critical roles in determining the response positions, FWHMs, and responsivities of OAL-OPDs. Based on the Beer–Lambert Law, the intensity of light passing through an object is directly associated with its molar extinction coefficient and light passing length, which is described as follows [43,44]:

$$I(\lambda) = I_{\mathrm{O}}(\lambda) \times 10^{-\varepsilon(\lambda)lc}, \tag{4}$$

where $I(\lambda)$ refers to the light intensity passing through the sample, I_{O} denotes the input light intensity, $\varepsilon(\lambda)$ denotes the molar extinction coefficient as a function of wavelength, l denotes the light path, and c indicates the concentration of the targeted solution. From a mathematical perspective, if the $\varepsilon(\lambda)$ is precisely known for an ideal organic semiconductor, it is feasible to accurately compute $I(\lambda)$ reaching in the OAL-OPD and thus the responsivity as a function of wavelength, offering reference for precisely designing narrowband OPDs with defined FWHMs. However, this is unfeasible in practice because of a general red shift in organic semiconductors from solutions to films due to the strong π–π stacking among molecules. Moreover, the broad absorption tail in organic semiconductor films generally results from disorders [45–47]. Thus, the real FWHM of the OAL-OPD depends on the practical absorption profile of the OAL layer with a defined thickness:

$$R_{\mathrm{OAL}}(\lambda) = R_{\mathrm{O}} \times \frac{I}{I_{\mathrm{O}}} = R_{\mathrm{O}}(\lambda) \times 10^{-\alpha(\lambda)l}, \tag{5}$$

where $R_{\mathrm{OAL}}(\lambda)$ refers to the responsivity of the OAL-OPD, $R_{\mathrm{o}}(\lambda)$ refers to the original responsivity of the OPD without OAL, and l and $\alpha(\lambda)$ are the thickness and absorption coefficient of the OAL films, respectively. Because organic semiconductors have extremely high absorption coefficients of over 10^5 cm^{-1}, ultrathin OALs with a thickness of less than 1 μm can totally absorb the undesired light.

We preliminarily hypothesized that the absorption onset, edge, tail of the OAL, and the response edge of the OPD simultaneously determined the peak response position, FWHM, and responsivity of OAL-OPDs. The response position of the OAL-OPD is determined by the absorption onset of the OAL, following the principle of $\lambda_{\mathrm{Peak\ responsivity}}$(OAL-OPD) = $\lambda_{\mathrm{Absorption\ onset}}$ (OAL), which is suitable for all OAL-OPDs prepared with PBDB-T:F-2F, as shown in Fig. 3d–f and Fig. S1. In the short-wavelength region, the incident light falls off exponentially in the OAL with a high $\alpha(\lambda)$, leading to few high-energy photons reaching the rear OPD and generating negligible photocurrent. Meanwhile, within the absorption tail of the OAL with low $\alpha(\lambda)$, incident photons propagate the OAL and reach the BHJ film, exciting acceptors to produce photocarriers. Thus, the OAL-OPD can detect a specific wavelength with energy close to the absorption tail of the acceptors.

Mathematically, the FWHM of the OAL-OPD can be approximated as follows: FWHM ≈ $\lambda_{\mathrm{Response\ onset}}$ (OAL-OPD) − $\lambda_{\mathrm{Absorption\ onset}}$ (OAL). The calculation results do not match well with the experimental data obtained in the OAL-OPD with different OALs because of the asymmetrical response curve of the OAL-OPD originating from the distinct slopes of the absorption edge of OALs and the response edge of the OPD. The absorption edge of the OAL indicates the first half of the response curve of OAL-OPDs, whereas the second half exhibits the response of the OPD (Fig. S1). With increasing F-2F fractions in OALs, the resulting FWHMs become closer to the calculation results.

In theory, the peak responsivity of the OAL-OPD should be identical to that of the original OPD if there is no additional optical absorption and reflection in the region beyond the absorption onset of the OAL, in contrast to the practical result obtained from OAL-OPDs. This inconsistency can be ascribed to the broad absorption tail of the OAL, which has a relatively low absorption coefficient and mainly absorbs low-energy incident photons. From Fig. 3e, f, OAL-OPDs prepared by OALs with PBDB-T:F-2F weight ratios of 10:3 and 10:6 exhibit the same response position of 785 nm and FWHMs of 30 nm but different peak responsivities of 0.15 and 0.07 A W^{-1}, respectively. The OAL with a higher F-2F content has a higher absorption coefficient in the long-wavelength region, absorbing more low-energy photons and thus suppressing the responsivity of the OAL-OPD. As shown in Fig. 3e, f, the second half of the OAL-OPD response curve deviates from the original OPD in the long-wavelength region, with increasing F-2F content in OAL, due to the strong absorption of the OAL in long wavelengths and thus suppressing the responsivity. Thus, in the OAL-OPDs, the OAL with a sharp absorption edge and narrow absorption tail can contribute to realizing narrow FWHMs and high responsivities.

At the molecular level, the OAL absorption edge and EQE tail are mainly influenced by the subband in organic films, arising from energetic disorders in blend films. Specifically, the absorption onset of the OAL is mainly determined by the narrowband semiconductor content, whereas the absorption tail is influenced by energetic disorders in the film. It is promising to control their optical characteristics by tuning the backbone, side chains, and end groups of narrowband acceptors to control their optical bandgap, packing mode, film morphology, and thus the absorption profile [48]. In addition, by controlling the film processing conditions, such as solvents, temperature, and post-treatment, it is feasible to tune the molecular packing and absorption profiles of organic semiconductors [45,49,50]. Thus, there are limitless possibilities for designing and fabricating narrowband OPDs with the required FWHMs and optoelectronic performance. Overall, realizing high-performance narrowband OPDs requires sharpening the absorption edge, narrowing the absorption tail of the OAL, and enhancing the responsivity and response edge of the OPDs. In the future, it is promising to predict the response windows and FWHMs of OAL-OPDs by characterizing the absorption profile of the OAL and the responsivities of OPDs before building OAL-OPDs, which offers invaluable insights into designing high-perfor-

mance OAL-OPDs.

Universality of the OAL strategies for narrowband OPDs

According to the working mechanism of OAL-OPDs, we finely selected eight additional acceptors with different bandgaps to explore the universality of the OAL strategy for narrowband OPDs, i.e., $PC_{71}BM$, F(Br)-ThCl, F-M, FO-2Cl, CH17, F8IC, 2,2′-[[4,4,11,11-tetrakis(4-hexylphenyl)-4,11-dihydrothieno-[2′,3′:4,5]thieno[2,3-*d*]thieno[2″″,3″″:4‴,5‴]thieno[2‴,3‴:4″,5″]pyrano[2″,3″:4′,5′]thieno[2′,3′:4,5]thieno[3,2-*b*]pyran-2,9-diyl]bis[methylidyne(5,6-difluoro) (COi_8DFIC), and SiOTIC (their chemical structures are shown in Fig. S2). In some cases, we also introduced external acceptors in OALs for complementary spectrum absorption, which have wider bandgaps than the acceptors used in OPDs (Fig. 4a). All of these acceptors display significantly high molar absorption efficiency over 10^5 mol^{-1} L cm^{-1} (Fig. S3a, b) in the range of 600–1000 nm (Fig. 4b). The energy diagrams of these acceptors were determined by cyclic voltammetry, and the results are shown in Fig. S4.

Based on their frontier molecule orbitals, donors with suitable energy levels were selected to construct high-performance OPDs

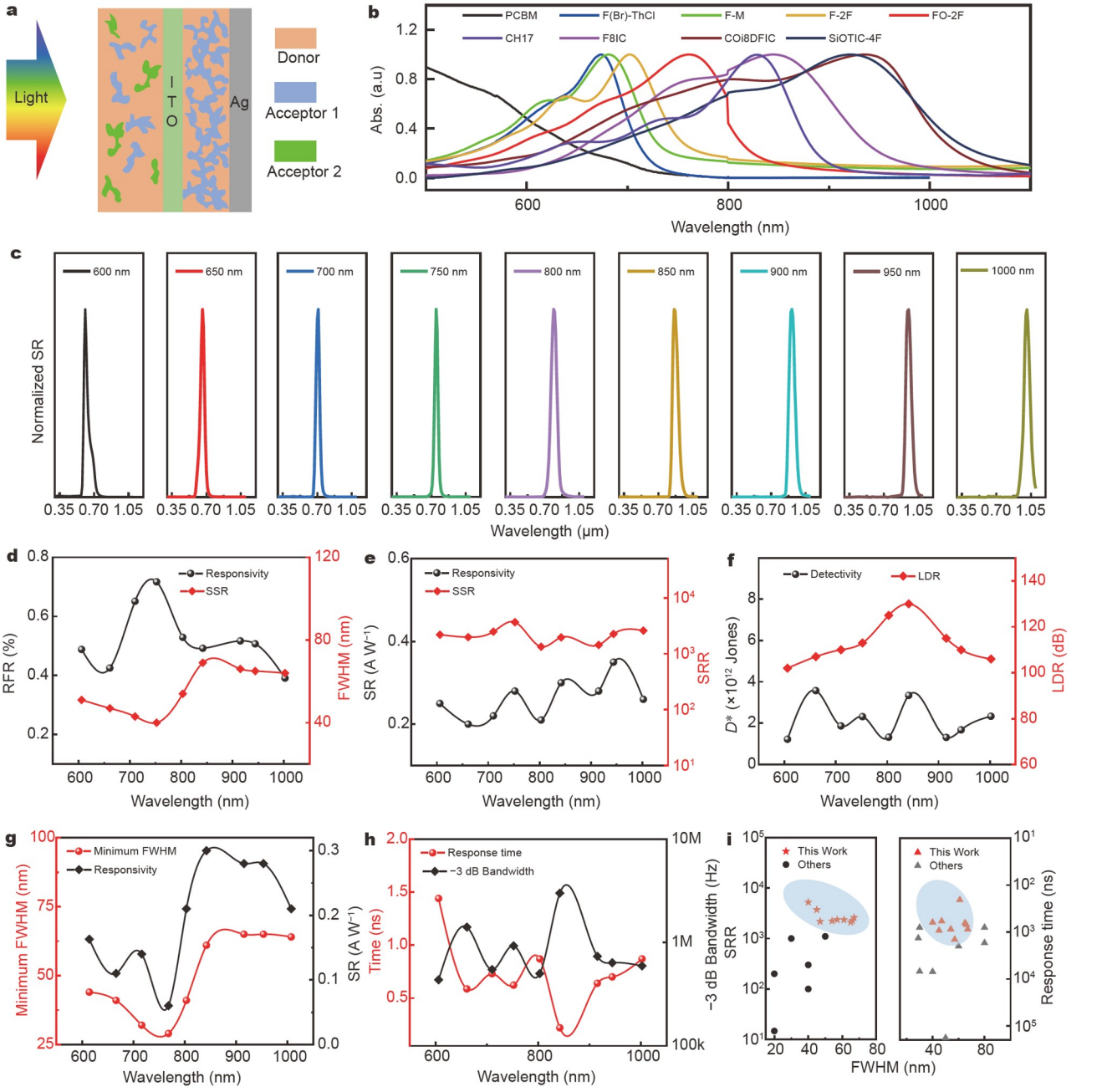

Figure 4 Optoelectronic performance of OAL-OPDs. (a) Schematic of OAL-OPDs. (b) Absorption profiles of acceptors. (c) Narrowband OPDs with different response windows in the range of 600–1000 nm. (d) Summary of RFR and FWHMs, (e) peak responsivity and SRR, and (f) the corresponding specific detectivities and LDRs of OAL-OPDs. (g) Minimum FWHMs of OAL-OPDs and their corresponding responsivities. (h) Response time and −3 dB cutoff frequencies of OAL-OPDs prepared with different acceptors. (i) Summary of SRR and response time of narrowband OPDs with different working mechanisms.

(Fig. S5). The detailed process for the fabrication and optimization of OPDs and OALs is outlined in the Supplementary information. Analogous to the OAL-OPD based on PBDB-T:F-2F, all OAL-OPDs prepared with different donors and acceptors display tunable FWHMs of 30–80 nm (Fig. 4c, Figs S6–S8 and Table S2). Details regarding the tunable FWHMs and their corresponding responsivities are listed in Table S2. As discussed above, RFR is preliminarily used to assess OAL-OPD performance. As shown in Fig. 4d, all of these OAL-OPDs show high RFRs of over 5 mA W^{-1} nm^{-1} with outstanding narrowband photoresponse over a broad spectrum of 600–1000 nm (Fig. S9), centering at specific wavelengths of 606, 661, 710, 750, 803, 842, 908, 946, and 1007 nm, with the corresponding FWHMs of 51, 47, 36, 40, 40, 61, 60, 61, and 61 nm, respectively (Table S2). Furthermore, the SRR and responsivities of these optimized OAL-OPDs are over 1000 and above 0.2 A W^{-1}, respectively.

Interestingly, the response edge of the OPD plays a critical role in determining the FWHM and responsivity of OAL-OPDs. From Fig. S10, the F-2F-based OAL-OPDs with a response slope of −0.010 A W^{-1} nm^{-1} show a narrow FWHM of 40 nm with the corresponding peak responsivity of 0.3 A W^{-1}. Meanwhile, OAL-OPDs prepared with CH17, F8IC, and CO*i*8DFIC, with relatively close responsivities of 0.3 A W^{-1}, have smaller response slopes of −0.006, −0.007, and −0.006 A W^{-1} nm^{-1},

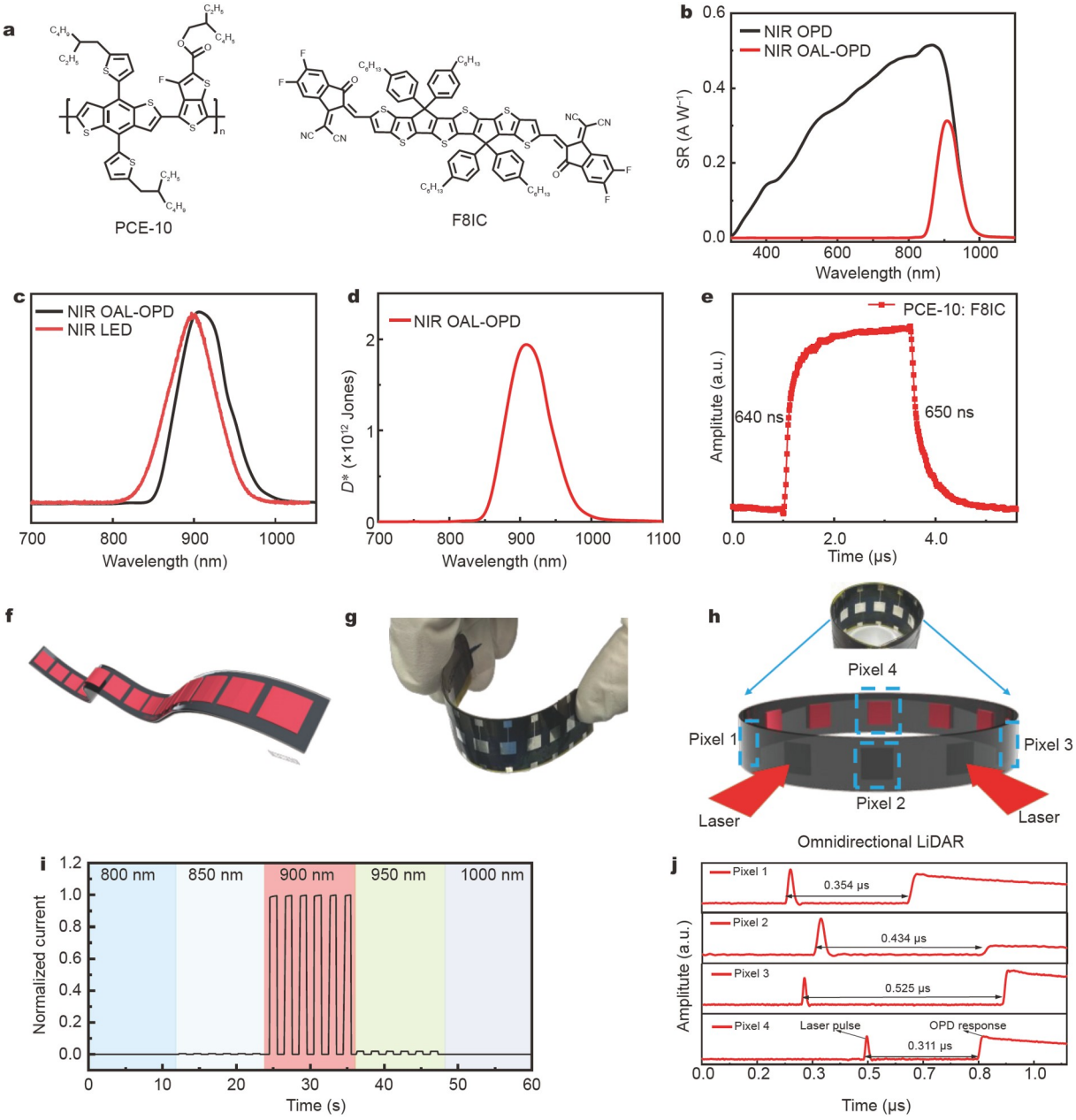

Figure 5 Omnidirectional LiDAR based on the flexible PD array. (a) Chemical structures of PCE-10 and F8IC. (b) Responsivities of broadband and narrowband NIR OPD. (c) Spectral profiles of LED and narrowband NIR OPD. (d) Specific detectivity of narrowband NIR OPD. (e) Response time of narrowband NIR OPD. (f) Schematic of the flexible narrowband PD array and omnidirectional LiDAR. (g, h) Optical images and schematic of the flexible narrowband OPD linear array (90 mm × 17 mm). (i) Spectral selectivity of OAL-OPD prepared with PCE-10:F8IC BHJ film and PM6:CH17 OAL. (j) Time delay between laser and OPD response from pixels 1–4 in (h).

with higher FWHMs of 66, 66, and 65 nm, respectively.

All these OAL-OPDs exhibit strong capabilities for weak light detection with significantly high specific detectivities of over 10^{12} Jones and remarkable environmental adaptability with large LDRs of over 100 dB due to low dark currents and high responsivities of OAL-OPDs (Figs S11 and S12). Significantly, the minimum FWHMs of all these OAL-OPDs are below 70 nm with a responsivity above 0.2 A W^{-1}. Compared with previous thick narrowband OPDs with response times at the microsecond level, all OAL-OPDs prepared with non-fullerene acceptors display short response times of less than 950 ns (Fig. 4h and Fig. S13), with a corresponding −3 dB cutoff frequency of over 500 kHz, as plotted in Fig. 4h and Fig. S14. In Fig. 4i and Fig. S15, the OAL-OPD presents significantly higher SRR and faster response speed than previous narrowband OPDs with different working mechanisms, efficiently addressing the issue of slow response and poor spectral selectivity in narrowband OPDs. It is worth noting that OAL-OPDs have superior optoelectronic performance across all critical parameters of narrowband OPDs, as summarized in Table S2. The outstanding optoelectronic performance, as well as the universal fabrication technique, paves the way for large-scale fabrication of narrowband OPDs by wet chemistry methods under ambient condition.

Omnidirectional LiDAR based on the flexible narrowband PD array

LiDAR is utilized in autonomous vehicles, machine vision, and augmented reality and works by measuring the time it takes for a short-pulsed light to pass between a target object and the detector. For challenging applications, it is critical to realize highly selective and sensitive NIR light detection without environmental light interference. Furthermore, it is imperative to realize 360° scanning without mechanical rotation, which requires flexible PDs to detect omnidirectional light reflected from targets. In this study, we developed a flexible narrowband NIR OAL-OPD linear array in which PM6:CH17 and PCE-10:F8IC worked as the OAL and photoactive film, respectively, as shown in Fig. 5a and Fig. S16. The detailed fabrication process is illustrated in the Supplementary information. Here, the OAL-OPD was prepared with the PM6:CH17-based OAL with a weight ratio of 10:6, which shows an FWHM of 65 nm centered at 905 nm, matching well with the NIR light source employed in the LiDAR system (Fig. 5c and Fig. S17). In addition, the OAL-OPD shows a high specific detectivity of over 10^{12} Jones, a response time of around 650 ns, and remarkable mechanical stability, ensuring its applications in flexible omnidirectional LiDAR (Fig. 5d, e). In Fig. 5g, h, a narrow PD linear array with 12 OPD units is evenly distributed on a flexible PET substrate (90 mm × 17 mm), which can wrap on a cylinder, enabling 360° detection without the need for mechanical rotation, as depicted in Fig. 5h. Fig. 5i presents that the NIR OAL-OPD displays significantly high spectrum selectivity, with a prominent peak centered at 900 nm and negligible interference from visible light and NIR light above 950 nm. Based on the TOF, an average of 60.9 m was detected from pixels 1–4 in Fig. 5j. Also, the flexible narrowband OPD has minimal performance degradation regarding responsivity, response speed, and dark current after undergoing 450 bending cycles (Fig. S18).

CONCLUSIONS

In this work, a facile and universal solution-processed strategy was proposed to construct high-performance narrowband OPDs for arbitrary narrow spectrum detection in the 600–1000 nm region. This remarkable performance was realized by introducing an organic OAL made from the same components as those of photoactive films. By finely adjusting the D:A weight ratio in OALs, we precisely tuned the FWHMs (minimum narrowing step of 2 nm) and response positions in OAL-OPDs. The obtained narrowband OPD exhibited remarkable comprehensive optoelectronic performance, including a narrow FWHM of 40 nm centered at 750 nm, responsivity of 0.28 A W^{-1}, −3 dB cutoff bandwidth of 927 kHz, and specific detectivity of over 10^{12} Jones, which are recorded in self-powered narrowband OPDs. In addition, this facile and straightforward method shows significant universality for all OPDs with arbitrary narrow spectral responses from 600–1000 nm with exceptional optoelectronic performance. We found that the performance of OAL-OPDs, i.e., FWHM, responsivity, and response windows, was mainly determined by the absorption onset, absorption tail, and slope of the absorption edge of the OAL, as well as the slope of the EQE edge of the OPD. These results offer practical guidelines for designing narrowband OPDs for the arbitrary spectral detection. Benefiting from the intrinsic flexibility and outstanding optoelectronic performance of the OAL-OPD, we fabricated a flexible narrowband OPD linear array for use in omnidirectional LiDAR for a 360° detection without mechanical rotation. We imagine that this practical and facile strategy, coupled with the exceptional performance of narrowband OPDs and ease of solution processing, will speed up the commercialization of flexible narrowband OPDs and expand their applications in various fields, such as imaging, optical communication, and spectrometers.

Received 11 October 2023; accepted 3 January 2024; published online 20 February 2024

1 Lin Q, Armin A, Burn PL, *et al.* Filterless narrowband visible photodetectors. Nat Photon, 2015, 9: 687–694
2 Armin A, Jansen-van Vuuren RD, Kopidakis N, *et al.* Narrowband light detection *via* internal quantum efficiency manipulation of organic photodiodes. Nat Commun, 2015, 6: 6343
3 Xie B, Xie R, Zhang K, *et al.* Self-filtering narrowband high performance organic photodetectors enabled by manipulating localized Frenkel exciton dissociation. Nat Commun, 2020, 11: 2871
4 Li Z, Yan T, Fang X. Low-dimensional wide-bandgap semiconductors for UV photodetectors. Nat Rev Mater, 2023, 8: 587–603
5 Morteza Najarian A, Vafaie M, Johnston A, *et al.* Sub-millimetre light detection and ranging using perovskites. Nat Electron, 2022, 5: 511–518
6 Kim I, Martins RJ, Jang J, *et al.* Nanophotonics for light detection and ranging technology. Nat Nanotechnol, 2021, 16: 508–524
7 Zhu Y, Geng C, Hu L, *et al.* Skin-like near-infrared II photodetector with high performance for optical communication, imaging, and proximity sensing. Chem Mater, 2023, 35: 2114–2124
8 Bao J, Bawendi MG. A colloidal quantum dot spectrometer. Nature, 2015, 523: 67–70
9 Yang Z, Albrow-Owen T, Cui H, *et al.* Single-nanowire spectrometers. Science, 2019, 365: 1017–1020
10 Deng W, Zheng Z, Li J, *et al.* Electrically tunable two-dimensional heterojunctions for miniaturized near-infrared spectrometers. Nat Commun, 2022, 13: 4627
11 Vanderspikken J, Maes W, Vandewal K. Wavelength-selective organic photodetectors. Adv Funct Mater, 2021, 31: 2104060
12 Yoon S, Sim KM, Chung DS. Bifunctional etalon-electrode to realize high-performance color filter free image sensor. ACS Nano, 2019, 13: 2127–2135
13 Liu J, Yi K, Wang Z, *et al.* All-organic composites with strong photo-

electric response over a wide spectral range. Sci China Mater, 2021, 64: 1197–1205
14 Zhao B, Wang F, Chen H, *et al.* Solar-blind avalanche photodetector based on single ZnO–Ga_2O_3 core–shell microwire. Nano Lett, 2015, 15: 3988–3993
15 Strobel N, Droseros N, Köntges W, *et al.* Color-selective printed organic photodiodes for filterless multichannel visible light communication. Adv Mater, 2020, 32: 1908258
16 Li G, Suja M, Chen M, *et al.* Visible-blind UV photodetector based on single-walled carbon nanotube thin film/ZnO vertical heterostructures. ACS Appl Mater Interfaces, 2017, 9: 37094–37104
17 Ollearo R, Ma X, Akkerman HB, *et al.* Vitality surveillance at distance using thin-film tandem-like narrowband near-infrared photodiodes with light-enhanced responsivity. Sci Adv, 2023, 9: eadf9861
18 Hu PA, Wang L, Yoon M, *et al.* Highly responsive ultrathin GaS nanosheet photodetectors on rigid and flexible substrates. Nano Lett, 2013, 13: 1649–1654
19 Hu PA, Wen Z, Wang L, *et al.* Synthesis of few-layer GaSe nanosheets for high performance photodetectors. ACS Nano, 2012, 6: 5988–5994
20 Dai M, Chen H, Feng R, *et al.* A dual-band multilayer InSe self-powered photodetector with high performance induced by surface plasmon resonance and asymmetric Schottky junction. ACS Nano, 2018, 12: 8739–8747
21 Wang Y, Kublitski J, Xing S, *et al.* Narrowband organic photodetectors—Towards miniaturized, spectroscopic sensing. Mater Horiz, 2022, 9: 220–251
22 Zhu Y, Chen H, Han R, *et al.* High-speed flexible near-infrared organic photodiode for optical communication. Natl Sci Rev, 2023, nwad311
23 Liu Q, Zeiske S, Jiang X, *et al.* Electron-donating amine-interlayer induced n-type doping of polymer:nonfullerene blends for efficient narrowband near-infrared photo-detection. Nat Commun, 2022, 13: 5194
24 Argence B, Chanteau B, Lopez O, *et al.* Quantum cascade laser frequency stabilization at the sub-Hz level. Nat Photon, 2015, 9: 456–460
25 Lukac R. Single-sensor imaging in consumer digital cameras: A survey of recent advances and future directions. J Real-Time Image Proc, 2006, 1: 45–52
26 Hu Y, Dai M, Feng W, *et al.* Monolayer hydrophilic MoS_2 with strong charge trapping for atomically thin neuromorphic vision systems. Mater Horiz, 2020, 7: 3316–3324
27 Dai M, Wang Z, Wang F, *et al.* Two-dimensional van der Waals materials with aligned in-plane polarization and large piezoelectric effect for self-powered piezoelectric sensors. Nano Lett, 2019, 19: 5410–5416
28 Xing S, Nikolis VC, Kublitski J, *et al.* Miniaturized vis-NIR spectrometers based on narrowband and tunable transmission cavity organic photodetectors with ultrahigh specific detectivity above 10^{14} Jones. Adv Mater, 2021, 33: 2102967
29 Dai M, Chen H, Wang F, *et al.* Robust piezo-phototronic effect in multilayer γ-InSe for high-performance self-powered flexible photodetectors. ACS Nano, 2019, 13: 7291–7299
30 Gong X, Tong M, Xia Y, *et al.* High-detectivity polymer photodetectors with spectral response from 300 nm to 1450 nm. Science, 2009, 325: 1665–1667
31 Yang J, Huang J, Li R, *et al.* Cavity-enhanced near-infrared organic photodetectors based on a conjugated polymer containing [1,2,5]selenadiazolo[3,4-*c*]pyridine. Chem Mater, 2021, 33: 5147–5155
32 Yan T, Li Z, Cao F, *et al.* An all-organic self-powered photodetector with ultraflexible dual-polarity output for biosignal detection. Adv Mater, 2022, 34: 2201303
33 Gao L, Ge C, Li W, *et al.* Flexible filter-free narrowband photodetector with high gain and customized responsive spectrum. Adv Funct Mater, 2017, 27: 1702360
34 Wang W, Zhang F, Du M, *et al.* Highly narrowband photomultiplication type organic photodetectors. Nano Lett, 2017, 17: 1995–2002
35 Xing S, Wang X, Guo E, *et al.* Organic thin-film red-light photodiodes with tunable spectral response *via* selective exciton activation. ACS Appl Mater Interfaces, 2020, 12: 13061–13067
36 Li L, Deng Y, Bao C, *et al.* Self-filtered narrowband perovskite photodetectors with ultrafast and tuned spectral response. Adv Opt Mater, 2017, 5: 1700672
37 Meng L, Liang H, Song G, *et al.* Tandem organic solar cells with efficiency over 19% *via* the careful subcell design and optimization. Sci China Chem, 2023, 66: 808–815
38 Meng L, Yi YQQ, Wan X, *et al.* A tandem organic solar cell with PCE of 14.52% employing subcells with the same polymer donor and two absorption complementary acceptors. Adv Mater, 2019, 31: 1804723
39 Ke X, Meng L, Wan X, *et al.* The rational and effective design of nonfullerene acceptors guided by a semi-empirical model for an organic solar cell with an efficiency over 15%. J Mater Chem A, 2020, 8: 9726–9732
40 Chen H, Zou Y, Liang H, *et al.* Lowing the energy loss of organic solar cells by molecular packing engineering *via* multiple molecular conjugation extension. Sci China Chem, 2022, 65: 1362–1373
41 Zhao Z, Xu C, Ma Y, *et al.* Ultraviolet narrowband photomultiplication type organic photodetectors with Fabry–Pérot resonator architecture. Adv Funct Mater, 2022, 32: 2203606
42 Wang X, Pan Y, Xu Y, *et al.* High spectral-rejection-ratio narrowband photodetectors based on perovskite heterojunctions. Adv Elect Mater, 2022, 8: 2200178
43 Yazmaciyan A, Meredith P, Armin A. Cavity enhanced organic photodiodes with charge collection narrowing. Adv Opt Mater, 2019, 7: 1801543
44 Tang Z, Ma Z, Sánchez-Díaz A, *et al.* Polymer:fullerene bimolecular crystals for near-infrared spectroscopic photodetectors. Adv Mater, 2017, 29: 1702184
45 Chen H, Liang H, Guo Z, *et al.* Central unit fluorination of nonfullerene acceptors enables highly efficient organic solar cells with over 18 % efficiency. Angew Chem Int Ed, 2022, 61: e202209580
46 Liang H, Chen H, Wang P, *et al.* Molecular packing and dielectric property optimization through peripheral halogen swapping enables binary organic solar cells with an efficiency of 18.77%. Adv Funct Mater, 2023, 33: 2301573
47 Chen H, Zhang Z, Wang P, *et al.* 3D acceptors with multiple A–D–A architectures for highly efficient organic solar cells. Energy Environ Sci, 2023, 16: 1773–1782
48 Wan X, Li C, Zhang M, *et al.* Acceptor–donor–acceptor type molecules for high performance organic photovoltaics—Chemistry and mechanism. Chem Soc Rev, 2020, 49: 2828–2842
49 Yao Z, Liao X, Gao K, *et al.* Dithienopicenocarbazole-based acceptors for efficient organic solar cells with optoelectronic response over 1000 nm and an extremely low energy loss. J Am Chem Soc, 2018, 140: 2054–2057
50 Xiao Z, Jia X, Li D, *et al.* 26 mA cm^{-2} J_{sc} from organic solar cells with a low-bandgap nonfullerene acceptor. Sci Bull, 2017, 62: 1494–1496

Acknowledgements This work was supported by the National Key R&D Program of China (2022YFA1203304), the Minstry of Science and Technology of China (2022YFB4200400 and 2019YFA0705900), and the National Natural Science Foundation of China (21935007 and 52025033).

Author contributions Chen Y and Li G conceived and designed the project. Zhu Y fabricated the narrowband photodetector and carried out all of the performance studies. The manuscript was mainly written by Chen Y, Li G, and Zhu Y. All authors contributed in the general discussion.

Conflict of interest The authors declare that they have no conflict of interest.

Supplementary information Experimental details and supporting data are available in the online version of the paper.

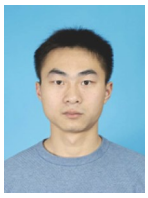

Yu Zhu received his Bachelor degree from Lanzhou University in 2019. He is currently a PhD candidate at Nankai University. His research mainly focuses on the design and fabrication of photodetectors.

Guanghui Li received his PhD degree in chemical and environmental engineering from the University of California, Riverside in 2018. Currently, he is an associate professor of chemistry at Nankai University. His research interests primarily focus on nanomaterials and organic functional materials for photosensors.

Yongsheng Chen received his PhD degree in chemistry from the University of Victoria in 1997. From 2003, he has been a chair professor at Nankai University. His main research interests focus on carbon-based nanomaterials and organic functional materials for green energy applications.

一种实现任意窄带光谱检测的有机光电探测器通用策略

朱玉[1], 秦灏[1], 郭婷婷[1], 杨艳青[1], 张哲[1], 张京[1], 李明朋[1], 陈红滨[1], 吴思敏[1], 韩蕊蕚[1], 万相见[1], 李光辉[1*], 陈永胜[1,2*]

摘要 窄带光电探测器因其优异的综合性能，在光谱仪、激光雷达、光通信和监控等关键应用领域广受欢迎. 尽管窄带硅基探测器在当前市场上占据主导地位，但其本征刚性、光学带隙固定和尺寸大的特性极大地限制了其在新兴领域的应用，尤其是在柔性和可穿戴光电子领域. 在本工作中，我们报道了一种构筑窄带有机光电探测器(OPD)的简单通用策略. 该策略通过溶液法将活性层中的给体和受体材料制备成光学调制层(OAL)，并集成在OPD上，可实现对任意光谱的检测. 利用该策略，我们成功地构筑了以750 nm为中心的窄带OPD，其半峰宽(FWHM)为40 nm，光谱响应率为3667，−3 dB截止频率为927 kHz，打破了自驱动窄带OPD的性能记录. 值得注意的是，这种新颖的OAL策略在OPD中具有良好的通用性，可以实现对600至1000 nm范围内的任意窄光谱检测，具有 FWHM可调(最小步长为2 nm)、响应度和探测率高、响应速度快的优势. 受益于有机半导体固有的柔性特性，我们构筑了一种柔性且可弯曲的窄带近红外OPD线性阵列，并应用于全向激光雷达上，在无需机械旋转的情况下实现了360°水平扫描.